



저작자표시-비영리-변경금지 2.0 대한민국

이용자는 아래의 조건을 따르는 경우에 한하여 자유롭게

- 이 저작물을 복제, 배포, 전송, 전시, 공연 및 방송할 수 있습니다.

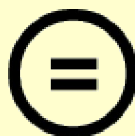
다음과 같은 조건을 따라야 합니다:



저작자표시. 귀하는 원저작자를 표시하여야 합니다.



비영리. 귀하는 이 저작물을 영리 목적으로 이용할 수 없습니다.



변경금지. 귀하는 이 저작물을 개작, 변형 또는 가공할 수 없습니다.

- 귀하는, 이 저작물의 재이용이나 배포의 경우, 이 저작물에 적용된 이용허락조건을 명확하게 나타내어야 합니다.
- 저작권자로부터 별도의 허가를 받으면 이러한 조건들은 적용되지 않습니다.

저작권법에 따른 이용자의 권리는 위의 내용에 의하여 영향을 받지 않습니다.

이것은 [이용허락규약\(Legal Code\)](#)을 이해하기 쉽게 요약한 것입니다.

[Disclaimer](#) 

Master's Thesis

Hybrid Electrode Architecture for High-Performance Seawater Batteries

Dae-Hyeon Jeong

Department of Energy Engineering
(Battery Science and Technology)

Graduate School of UNIST

2018

Hybrid Electrode Architecture for High-Performance Seawater Batteries

Dae-Hyeon Jeong

Department of Energy Engineering
(Battery Science and Technology)

Graduate School of UNIST

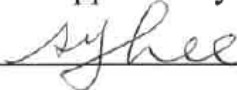
Hybrid Electrode Architecture for High-Performance Seawater Batteries

A thesis/dissertation
submitted to the Graduate School of UNIST
in partial fulfillment of the
requirements for the degree of
Master of Science

Dae-Hyeon Jeong

12/12/2017

Approved by



Advisor

Sang-Young Lee

Hybrid Electrode Architecture for High-Performance Seawater Batteries

Dae-Hyeon Jeong

This certifies that the thesis/dissertation of **Dae-Hyeon Jeong**
is approved.

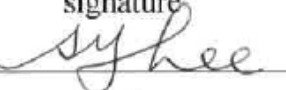
12/12/2017

signature



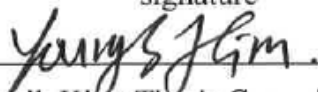
Advisor: Sang-Young Lee

signature



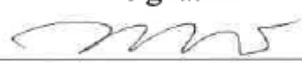
Sang-Young Lee: Thesis Committee Member #1

signature



Youngsik Kim: Thesis Committee Member #2

signature



Guntae Kim: Thesis Committee Member #3

Contents

I. Introduction -----	7
II. Result -----	
2.1 Fibrous Nanomat Hard-Carbon anode -----	11
2.2 1D Bucky Paper cathode -----	19
2.3 FNHC/1DBP Seawater Full Cell -----	25
III. Discussion -----	27
IV. Supplementary Information -----	32
V. References and Notes -----	41

Hybrid Electrode Architecture for High-Performance Seawater Batteries

Dae-Hyeon Jeong and Sang-Young Lee*

The continuous throng in demand for high energy density rechargeable batteries innovatively drives technological development in cell design as well as electrochemically active materials. In that perspective metal-free batteries consisting of a flowing seawater as a cathode active material were introduced. However, the electrochemical performance of the seawater battery was restrained by NASICON ($\text{Na}_3\text{Zr}_2\text{Si}_2\text{PO}_{12}$) ceramic solid electrolyte. Here, we demonstrate a new class of fibrous nanomat hard-carbon (FNHC) anode/1D (one-dimensional) bucky paper (1DBP) cathode hybrid electrode architecture in seawater battery based on 1D building block-interweaved hetero-nanomat frameworks. Differently from conventional slurry-cast electrodes, exquisitely designed hybrid hetero-nanomat electrodes are fabricated through concurrent dual electrospaying and electrospinning for the anode, vacuum-assisted infiltration for the cathode. HC nanoparticles are closely embedded in the spatially reinforced polymeric nanofiber/CNT hetero-nanomat skeletons that play a crucial role in constructing 3D-bicontinuous ion/electron transport pathways and allow to eliminate heavy metallic aluminum foil current collectors. Eventually the FNHC/1DBP seawater full cell, driven by aforementioned physicochemical uniqueness, shows exceptional improvement in electrochemical performance (Energy density = 693 Wh kg^{-1}), (Power density = 3341 W kg^{-1}) removing strong stereotype of ceramic solid electrolyte, which beyond those achievable with innovative next generation battery technologies.

INTRODUCTION

Unprecedented increasing demand for high performance portable electronics, electric vehicles (EVs) and smart grid with energy storage systems (ESSs) relentlessly pursuits advanced electrochemical properties of energy power sources.¹⁻² Undoubtedly, lithium ion batteries (LIBs), among various energy power sources, have been the most powerful and widespread electrochemical system and obviously garnered attention due to well-customized characteristics with good performance.³⁻⁴

However, still a lack of resources such as cobalt and lithium restrain further growth of the lithium ion batteries. More importantly, electrochemical properties of lithium ion batteries have been reported as saturated system due to long-term challenges by research field and industry to solve its disadvantages. Thus, many researches have explored battery technologies for alternatives to lithium, such as magnesium, sodium or aluminum.⁵⁻⁶ Sodium, one of the alternatives, possess advantages, such as natural abundance and low cost. Fundamentally, the thermodynamically reversible storage mechanisms for sodium ions have high similarity to those for lithium ions. Furthermore, the voltage and cycle stability of sodium ion batteries are considerably competitive with those of LIBs.⁷⁻¹⁰

Meanwhile, new battery chemistries utilizing oxygen as active cathode species were introduced as a trend, sodium has recently paid attention as a potential replacement for lithium in these metal air batteries. Such batteries are promising energy storage system that provide very high theoretical energy densities.¹¹⁻¹⁵ However, anodes using pure alkali metals create safety and cost issues associated with their reactivity and expense of the required dry-assembly process. To address these issues, Kim's group recently set up an novel energy storage system using seawater as an abundant sodium source.¹⁶ Naturally abundant seawater usage as sodium

source retrenches unnecessary additional processing and substantial reduction of manufacturing cost. However, several researches over last few years have encountered numerous problems, such as eletrocatalytic performance of cathode material which affects poor electrochemical properties and insufficient cycle life with low discharge capacity of ceramic solid electrolytes such as NASICON ($\text{Na}_3\text{Zr}_2\text{Si}_2\text{PO}_{12}$).¹⁷⁻¹⁸

Ceramic solid electrolytes are brittle because of low fracture energies, high impedance grain boundaries and interfacial resistance of particles in compacted disks. Therefore, they fail to form conformal surfaces with electrode particles during charging and discharging which effectively leads to a high interfacial resistance, consequently derive deadly poor rate capabilities.¹⁸⁻¹⁹ Although most of research efforts have been dealing with ceramic membrane perspective to overcoming intrinsic disadvantages of ceramic solid electrolytes, none of them achieved satisfactory for their electrochemical performances.²⁰⁻²³ However, it still has been widely applied despite of its disadvantages against further development of sodium ion batteries.

Here, we introduce new direction for next generation seawater batteries. Interestingly we approached with electrode architecting perspective to resolve abovementioned problems. Conventional electrode structure consisted of a random mixture of active materials, carbon-based additives and polymer binders on the metallic foil current collectors.²⁴ Unfortunately, this simple stack-up structure of electrode often brings uneven and stagnant ion and electron transport in the vertical direction and even dimensional disruption upon mechanical deformation.²⁵⁻²⁶ Moreover, the presence of electrochemically inert materials such as binders, carbon-based additives and heavy metallic foil current collectors results in inevitable loss of areal capacity of the electrode because those account for a significant total mass portion.²⁷ Several approaches have conducted to make minimize those electrochemically inert materials,

for example, self-standing sheets based on active materials and conductive additives such as carbon nanofibers, carbon nanotubes and graphenes to facilitate ion/electron transport.²⁸⁻³⁰ The majority of these approaches have limitations of achieving both electrochemical performance and mechanical durability with manufacturing processability.

Here, we report a simple and functional electrode architecture design to address old-established challenges through demonstrating a new class of hybrid hetero-nanomat (Fibrous nanomat hard-carbon anode/1DBP carbon nanotube (CNT) cathode) seawater full cells based on 1D building block with interweaved hetero-nanomat frameworks. Development of 3D bicontinuous facile ion/electron transport networks and removal of metallic foil current collector. The nanomat electrodes are fabricated by a one-pot manufacturing process, *i.e.*, simultaneous electrospinning (for polymeric nanofibers), electrospaying (for active materials/CNTs)³¹⁻³² and vacuum-assisted infiltration (for CNT bucky papers).³³⁻³⁴

Owing to recent progress of electrospinning/electrospaying techniques, our group previously reported polyacrylonitrile (PAN) nanofiber/CNT-mediated LIB cathode to verify better performance than conventional slurry cast cathode.³¹⁻³² Our study suggests upgrade version of rechargeable power sources beyond state-of-art LIBs and especially, solutions for the break strong stereotype in terms of limitation of ceramic solid electrolyte.

In our FNHC anode, densely captured hard-carbon particles in interlocked polymeric nanofiber/CNT hybrid nanomat matrix, enable 3D bicontinuous facile ion transport and electron conduction channels which hasten electrochemical redox reaction kinetics inner structure of electrodes. In addition, highly reticulated CNT electronic networks allow significant increase in the areal capacity ($1.12 \text{ mAh cm}_{\text{anode}}^{-2}$) of electrode with removal of heavy metallic foil current collector.

Meanwhile, 1D bucky paper (hereinafter, simply referred to as “1DBP”) cathodes with highly compact 3D network composed of single wall carbon nanotube (SWCNTs) reticulated architecture exhibits unprecedented improvements in the electrochemical performance due to its structural/physicochemical uniqueness, which were not realized with conventional cathodes. Distinctive structure of densely packed SWCNTs allows spacious active surface area of active material for electrochemical reactions, which directly related to electrocatalytic oxygen evolution/reduction reactions. (OER/ORR). Also, uniform reticulated SWCNT networks in 1DBP cathodes improves electronic conductivity and enlarges porosity with well-defined pore diameter and ion/electron transport channels. Additionally, this well-defined pathway for ion and electron transport of 1DBP cathode boosts up electrochemical reaction kinetics even at harsh charge/discharge conditions.

Eventually aforementioned advanced hybrid nanomat electrode architecture with structural and electrochemical uniqueness shows unprecedented improvements of cell performance in seawater battery field. Especially, formidable rate capability, which are barely attained with ceramic solid electrolyte such as NASICON, eventually suggests a new innovation toward realization of advanced seawater batteries with ultrafast rate capability and ultrahigh energy density.

RESULT

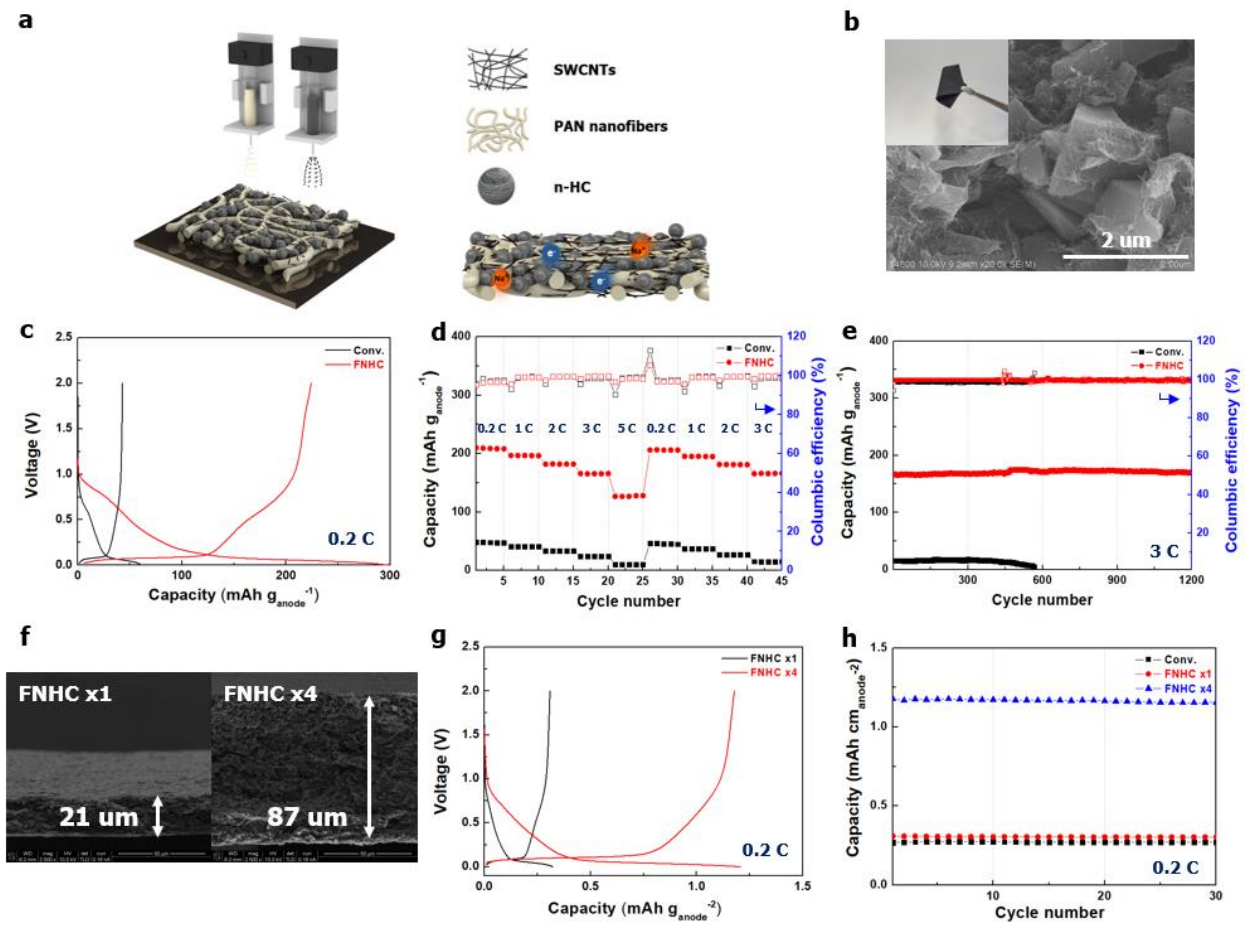


Fig. 1. Fabrication and characteristic morphology and electrochemical performance of FNHC anode. (a) Schematic illustration depicting the FNHC anode fabrication process. **(b)** SEM image of FNHC anode. The inset image shows a digital camera image (DCIM) of deformed FNHC anode. **(c)** Initial charge/discharge voltage profiles of anodes at charge/discharge current densities of 0.2 C/0.2 C, respectively. **(d)** Rate capability of anode half cells, FNHC anode vs. Conv. HC anode, where the charge/discharge current density was verified from 0.2 to 5.0 C, respectively. **(e)** Cycling performance of anode half cells, FNHC anode vs. Conv. HC anode, where the charge/discharge current densities of 3.0 C/3.0 C. **(f)** Cross-sectional SEM images of multi-stacked FNHC anode. **(g)** Initial charge/discharge

voltage profiles of multi-stacked FNHC anode at charge/discharge current densities of 0.2 C/0.2 C, respectively. **(h)** Cycling performance of anode half cells, multi-stacked FNHC anode vs. high-mass loading Conv. HC anode, where the charge/discharge current densities of 0.2 C/0.2 C.

Fabrication and morphology of FNHC anode

To fabricate the fibrous nanomat electrodes (hereinafter, simply referred to as “FN electrodes”), the HC powders (average diameter = 10 μm) were dispersed in isopropyl alcohol (IPA)/deionized water (D.I. water) (=3/7 (w/w)) co-solvent. Thoroughly important prerequisite for the electrospinning/electrospraying process was to guarantee no precipitation of active material particles in the dispersion solution. The bare hard-carbon powders (hereinafter, simply referred to as “b-HC”), due to their large particle size and density, were easily precipitated in the dispersion solution. To resolve this precipitation issue high energy mechanical milling (HEMM) was conducted.³⁵ The top-viewed SEM images (Fig. S1a-b, Supplementary Information) clearly showed that the particle size difference between b-HC and nano-sized hard-carbon (hereinafter, simply referred to as “n-HC”). The X-ray diffraction (XRD) patterns confirmed that b-HC’s characteristic XRD patterns clearly matching with n-HC’s XRD patterns (Fig. S1c, Supplementary Information). It indicated no deformations occurred with intrinsic property of b-HC even after HEMM.

The prepared n-HC particles were mixed with SWCNTs in the IPA/D.I. water co-solvent, wherein the ratio in composition of SWCNT/HC was 5/100 (w/w) and 0.4 wt% polyvinylpyrrolidone (PVP)³⁶ was used as a dispersing agent for SWCNT. Meanwhile, polyacrylonitrile (PAN) powders were dissolved in dimethyl formamide (DMF), wherein the

concentration of PAN was 10 wt%. The hard-carbon/SWCNT mixture solution and the PAN solution were respectively projected to concurrent electrospinning/electrospraying through two different nozzles (a schematic illustration was shown in Fig. 1a), thus producing n-HC particles embedded SWCNT/PAN FN electrodes sheet. After the PVP was eliminated by rinsing with D.I. water and followed ethanol, the FN electrode sheet was treated with calendaring process at room temperature and then thermally treated with 150 °C/2 h and 120 °C/12 h heating processes were followed for enhancing chemical durability of PAN nanofibers and then.³⁷⁻³⁸

Eventually, the self-standing FNHC anodes were obtained and the thickness was approximately to be 20 μm, which considerably thinner than that of conventional HC anodes, which was about 70 μm. From the initial composition ratio of HC/SWCNT, the X-ray photoelectron spectroscopy (XPS) data (Fig. S2a, Supplementary Information) and PAN nanofibers etching results (Fig. S2b, Supplementary Information), the composition ratio of the FNHC anodes was estimated to be (HC/SWCNT)/PAN = (67.5/3.4)/29.1 (w/w/w).

Physical structural uniqueness of FNHC anode

The schematic illustration clearly described FNHC anodes' unique structure and fabulously simple manufacturing process realized by dual electrospaying/electrospinning instrument (Fig. 1a). The top-viewed SEM image (Fig. 1b) clearly showed that the HC particles were closely packed in the electrospayed SWCNT/electrospun PAN nanofibers fibrous nanomat. This closely packed HC active materials formed totally different unique structure compared to morphologies of the previously reported conductive additive-/binder-/current collector-free electrodes which predominantly contributed to realizing high-capacity electrodes.²⁷ The representative examples included electrode binders replacing synthetic polymers such as

polyvinylidene fluoride (PVdF) and 3D porous layers decorated with electroconductive substances to replace conventional metallic current collectors as a mechanical buffer for metallic anode materials.

Furthermore, inset image of Fig. 1b obviously demonstrated flexible free standing gorgeous FNHC anodes. Remarkably, aluminum foil current collector, carbon-based powder conductive additives and nonconducting polymer binders such as polyvinylidene fluoride (PVdF), which were necessarily used for conventional electrodes, were not utterly found in the FNHC anodes. For a stark contrast between FNHC anodes and conventional HC anodes, the conventional HC anodes (HC/carbon black additive/PVdF binder = 80/10/10 (w/w/w) on a metallic aluminum foil current collector) were prepared as a control sample (Fig. S3a-b, Supplementary Information). The SEM image of FNHC anodes showed reticulated close-packed SWCNTs on the HC active material particles and unique porous morphology compared to that of conventional HC anodes so that it could achieve uniform and efficient transportation of electron/ion.

However, conventional HC anodes showed excessively densely packed surface SEM image which contained simple mixture of HC active material particles and carbon black additives as a conducting agent. Thus, it failed to form well defined electron/ion conduction pathway and less porosity induced sluggish electron/ionic transport kinetics. Eventually both three-dimensionally (3D) reticulated interstitial voids and elimination of carbon-based conducting agent powder/PVdF binders smoothly allowed much higher porosity than conventional anodes.

This porous structural uniqueness with suitable pore volume and pore diameter was proved by using N₂ physisorption isotherms analyzer (ASAP2420), (Fig. S4a, Supplementary Information). Figure S4a showed the N₂ adsorption-desorption isotherms of the FNHC anodes

and conventional HC anodes and additionally, the pore diameter distribution was calculated by the Barrett-Joyner-Halenda (BJH) method. The FNHC anodes had broad pore diameter distribution with comparatively large pore diameter (average pore diameter, $D_{\text{pore}} \sim 13.1$ nm). The broad pore diameter distribution was due to the presence of pores between the sub-constituent active materials (mesopores) and the internal voids within the individual section of FNHC anodes. The Brunauer-Emmett-Teller (BET) specific surface area (S_{BET}) and total pore volume (V_{pore}) were evaluated as $\sim 25.1 \text{ m}^2 \text{ g}^{-1}$ and $\sim 0.082 \text{ cm}^3 \text{ g}^{-1}$, respectively. In contrast, the conventional HC anodes had a narrow pore diameter distribution with relatively small pore diameter ($D_{\text{pore}} \sim 14.6$ nm). The S_{BET} and V_{pore} values were $1.29 \text{ m}^2 \text{ g}^{-1}$ and $0.004 \text{ cm}^3 \text{ g}^{-1}$, respectively. Therefore, the highly well-developed porous channels within FNHC anodes facilitated capillary encroachment of liquid electrolyte into the FNHC anodes (Fig. S5a, Supplementary Information). These results demonstrated that the SWCNT/PAN nanofibers-interlaced fibrous hetero-nanomat built up the well-formed ion/electron conduction pathway, which prevised to finally intensify electrochemical redox reaction kinetics of the FNHC anodes.

Electrochemical performance of FNHC anode

The FNHC anodes did not contain heavy metallic aluminum foil current collector, hence it enabled the high mass loading of active materials (Fig. S6a, Supplementary Information). Owing to elimination of the metallic aluminum foil current collector, the areal mass of the FNHC anodes was appreciably reduced compared to conventional HC anodes, wherein the areal active material mass loadings were well-nigh similar between the FNHC anodes and conventional HC anodes. As a consequence, the FNHC anodes allowed a formidable boost-up

in the gravimetric capacity (= capacity per anodes mass ($\text{mAh g}_{\text{anodes}}^{-1} = 210 \text{ mAh g}_{\text{anode}}^{-1}$)), (Fig. 1c).³⁹⁻⁴⁰

As SWCNT was used as both an electroconductive auxiliary agent and structural interconnecting supporting agent for FNHC anodes, specific contents of SWCNT crucially affected to the dispersion state of the suspension solutions (Fig. S7a, Supplementary Information). For SWCNT content of 5 wt%, the volumetric density of the SWCNTs was sufficiently high for constructing well-reticulated SWCNT networks. On the other hand, excessively high SWCNT content ($> 10 \text{ wt\%}$) resulted in the development of unexpected HC and SWCNT aggregates, which gave rise to severely poor dispersion state of the HC/SWCNT suspension solution. The apparent viscosity of HC/SWCNT suspension solution was investigated by analyzing its rheological properties (Fig. S7b, Supplementary Information).⁴¹ Higher apparent viscosity of the 10 wt% SWCNT compared to 5 wt% SWCNT could be attributed to the undesirable generation of the HC/SWCNT agglomeration.

To quantitatively elucidate the effect of the SWCNT content in the FNHC anodes, HC anodes sheets (HC nanoparticle/carbon black additive/PVdF binder = 80/10/10 (w/w/w)) were prepared using a typical slurry casting method (Fig. S7c, Supplementary Information). The electronic conductivities of the HC anodes increased proportionally with SWCNT contents. However, in the case of 10 wt% SWCNT, the electronic conductivity was severely ununiform because of inhomogeneity in the slurry casting process due to HC/SWCNT aggregation, which was unfavorable for electron transport in the electrode. Based on these results, the optimized SWCNT content for the HC/SWCNT suspension solution was suggested to be 5 wt%. In virtue of series of distinctive achievements FNHC anodes ($= 15.5 \text{ S cm}^{-1}$) attained substantially higher electronic conductivity than the conventional HC anodes ($= 2.2 \text{ S cm}^{-1}$), which was

attributed to the effect of the highly interconnected SWCNT networks within FNHC anodes due to low deformation energy of the SWCNT. (Fig. S7d, Supplementary Information).

Figure 1d showed that the FNHC anodes indicated significantly higher charge capacities (210 mAh g_{anode}^{-1} at 0.2 C) than the conventional HC anodes (48 mAh g_{anode}^{-1} at 0.2 C) over a wide range of charge/discharge current densities (from 0.2 to 5.0 C). The elimination of the heavy metallic aluminum foil current collector, in combination with the three-dimensionally reticulated higher ion-flux acceptable ion/electron transport channels, decisively contributed to outstanding improvement in the rate capability of the FNHC anodes. Exceptional accomplishment of the FNHC anodes was the high current density cycling performance (expressed as mAh g_{anodes}^{-1}), where the cells were tested at a high charge/discharge current density of 3.0 C/3.0 C under a voltage range of 0.1 – 2.0 V (Fig. 3e). The FNHC anodes exhibited much higher charge capacities (175 mAh g_{anode}^{-1}) and super stable capacity retention with cycling (98% after 1200 cycles), whereas the conventional HC anodes (15 mAh g_{anode}^{-1}) suffered from a sharp capacity fading after only 300 cycles. Peculiarly, the performance clearly proved that FNHC anodes had evenly distributed three-dimensional structure with well-embedded active materials, whereas the conventional electrodes contained substantial electrochemically disruptive binders. Furthermore, the abovementioned excellent electrochemical performance results were demonstrated again in form of specific gravimetric capacity (= capacity per active material mass (mAh g_{HC}^{-1}), (Fig. S8a-b, Supplementary Information). Not only high current density cycling performance but also normal charge/discharge current density (0.2 C/0.2 C under a voltage range of 0.1 – 2.0 V) cycling performance were also investigated (Fig.S8c-d, Supplementary Information). Driven by the preceding architectural/electrochemical uniqueness, the superb FNHC anodes showed

noteworthy improvement in electrochemical performance.

High energy density with multi-stacking FNHC anodes

The FN electrode-induced structural uniqueness of the FNHC anodes was anticipated to render a new opportunity for realizing ultrahigh-mass loading anodes that beyond those achievable with conventional electrode technology. The elimination of metallic aluminum foil current collector with distinctively unique nanomat architecture could allow facile fabrication for super high-mass loading, by multi-stacking FNHC anodes in series, which cross-sectional SEM images were exhibited in Figure 1f. The FNHC anodes in diverse stack-class were fabricated by simply stacking the number of fibrous nanomat anodes sheets ($21\ \mu\text{m}$ (= 1 sheet), $87\ \mu\text{m}$ (= 4 sheet)). The single layer of FNHC anodes sheets were stacked in series and then subjected to calendaring process in pursuance of ensured tightly interlinked interface between the adjoined anodes sheets. It is of note that, even FNHC anodes sheets were quadruple-stacked, which had thickness of $87\ \mu\text{m}$, the reticulated fibrous nanomat unique structure was well preserved in the whole-through-thickness direction.

The multi-stacked FNHC anodes displayed extraordinary advancement in the area capacity perspective. Proportionally to thickness of the FNHC anodes, the charge capacities per anodes area ($\text{mAh cm}_{\text{anodes}}^{-2}$) have distinct increasing propensity (Fig. 1g). Not only single layer of FNHC anodes but also quadruple-stacked FNHC anodes demonstrated vastly stable charge/discharge voltage profile (Fig. 1g). Furthermore, in normal charge/discharge current density of $0.2/0.2\ \text{C}$, the areal capacity of the quadruple-stacked FNHC anodes was in vicinity of $1.2\ \text{mAh cm}_{\text{anodes}}^{-2}$, which was a singularly remarkable enhancement that compared to that of the conventional HC anodes, which was approximately $0.25\ \text{mAh cm}_{\text{anodes}}^{-2}$ (Fig. 1h).

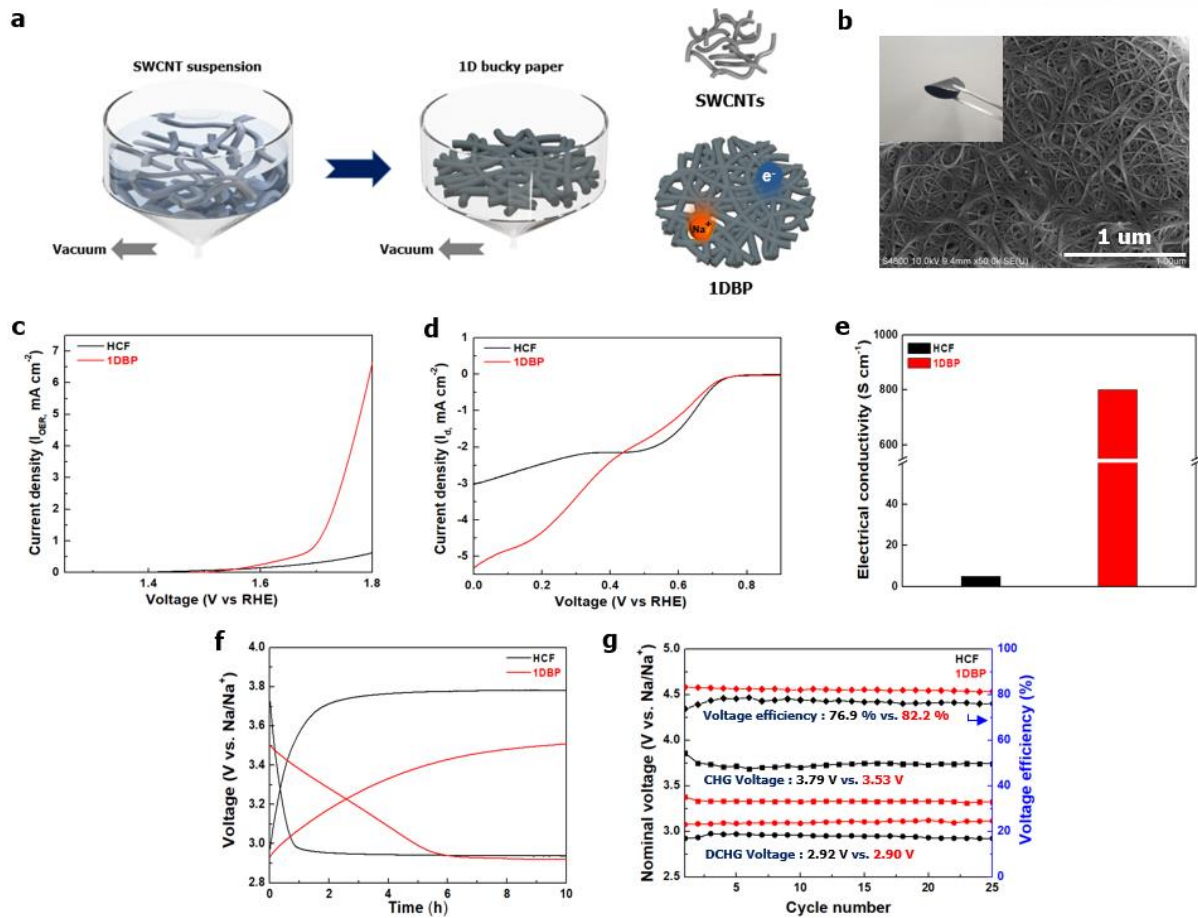


Fig. 2. Fabrication and characteristic morphology and electrocatalytic and electrochemical performance of 1DBP cathode. (a) Schematic illustration depicting the 1D bucky paper (1DBP) cathode fabrication process. (b) SEM image of 1DBP cathode. The inset image shows a digital camera image (DCIM) of deformed 1DBP cathode. (c) Oxygen evolution reaction (OER) disk currents of cathodes. (d) Oxygen reduction reaction (ORR) disk currents of cathodes. (e) Comparison of the electronic conductivities between the HCF and 1DBP cathodes. (f) Initial charge/discharge voltage profiles of a cathode half cells at a current density of 0.01 mA cm^{-2} . (g) The nominal charge/discharge voltages and voltage efficiency of seawater cathode half cells during cycling.

Fabrication and morphology of 1D bucky paper cathode

On the other hand, in the case of cathodes, herein we demonstrated unique nanomat 1D building block bucky paper (hereinafter, simply referred to as “1DBP”) based on highly compact 3D network of SWCNT reticulating architecture (Fig. 2a-b). The 1DBP cathodes were fabricated via a greatly simple vacuum-assisted infiltration process, which was similar with a traditional paper-making method.⁴⁰ The detail procedure of fabrication process was described minutely as follows. To achieve a good dispersion state of SWCNTs suspension, sodium dodecyl sulfate (SDS)⁴² was added as a dispersing agent (0.4 wt% in water as solvent). The SWCNT suspension was poured into a filter paper located inside a Porcelain Buchner funnel and then subjected to vacuum infiltration, leading to the formation of 1DBP.

Eventually, after vacuum-drying (at 120 °C for 2 h) process, the self-standing and flexible 1DBP cathodes were obtained. Notably, this distinctive 1DBP cathodes with not only various diameters but also diverse thicknesses were easily fabricated, which precisely correspond to excellent scalability and simplicity of the previously mentioned vacuum infiltration-based 1D BP cathodes manufacturing process.⁴³⁻⁴⁶

Physical structural characteristics of 1D bucky paper cathode

An important requirement for cathodes was the acquisition of high porosity and well-defined pore diameter, which enabled facile electron/ion transport via the electrolyte.⁴⁷⁻⁴⁸ The pore diameter distribution of the 1DBP cathodes were quantitatively measured by using N₂ physisorption isotherms analyzer (ASAP2420), (Fig. S9a, Supplementary Information). The 1DBP cathodes had a well-defined pore diameter distribution ($D_{\text{pore}} \sim 7.5$ nm) with densely packed structure. Particularly from the pore diameter distribution results, the specific surface

area was estimated to be approximately $342 \text{ m}^2 \text{ g}^{-1}$. This formidable large specific surface area of IDBP cathodes exactly contributed to enlarging electrochemical active reaction site within the cathodes. In contrast, the conventional heated carbon felt (hereinafter, simply referred to as “HCF”) cathodes had an uneven pore distribution with excessively large pore diameter, so that it affected to the electrochemical performance of conventional HCF cathodes (Fig. S9a, S10a, Supplementary Information).⁴⁹⁻⁵⁰

In addition, specific surface area of conventional HCF cathodes was evaluated to be approximately $1.7 \text{ m}^2 \text{ g}^{-1}$. Consequently, it was considered that the conventional HCF cathodes were improper due to these exorbitant pore diameter and deficient active specific surface area, which essentially contributed to critical adverse effect for electrochemical system. Therefore, the conventional HCF cathodes which indwell fatal factors to electrochemical performance were considered as inappropriate for this system.

Electrocatalytic and Electrochemical performance of 1D bucky paper cathode

The 1D bucky paper cathodes, in this paper, we developed a new type of noticeably improved OER/ORR bifunctional electrocatalyst based on the as-synthesized original SWCNTs (hereinafter, simply referred to as “o-SWCNT”) without any complex purification process or additional electrocatalyst.⁵¹ Due to the acid oxidation purification technique can cause undesired additional disorders and defects. [52] Thus, we minutely designed bifunctional electrocatalytic performance from o-SWCNT without purification, in virtue of the residual metals common in bulk CNTs.⁵¹⁻⁵²

In principle, the SWCNTs themselves had an excellent oxygen reduction reaction (ORR) electrocatalytic activity.⁵³ Furthermore, o-SWCNT contained small amounts of residual

metallic irons originated from catalysts of industrial manufacturing process and nitrogen impurities, which clearly contributed to excellent oxygen evolution reaction (OER) electrocatalytic activity by facilitating the formation of catalytic active sites and boosting up the activity of the electrocatalyst. These, thus, allowed the 1DBP cathodes to show bifunctional OER/ORR catalytic activity, which revealed by thermal gravimetric analysis (TGA), inductively coupled plasma mass spectrometry (ICP-MS) and X-ray photoelectron spectroscopy.

In addition, the confocal Raman spectra were obtained with a 532 nm laser, wherein the spatial 2D maps were recorded with respect to the characteristic G-band ($1560\text{--}1630\text{ cm}^{-1}$) of the SWCNT (Fig. S11a, Supplementary Information).⁵⁴ Raman characterizations obviously demonstrated that both o-SWCNT and purified SWCNT (hereinafter, simply referred to as “p-SWCNT”) exhibited similar degrees of disorder in the graphitic structures. From the thermogravimetric analysis (TGA) measurement, the metallic iron impurities of o-SWCNT and p-SWCNT were estimated to be 2.8 wt% and 19.9 wt%, respectively (Fig. S12a-b, Supplementary Information). It demonstrated that the vigorous purification process effectively removed the metallic iron impurities as well as improved purity of o-SWCNT. The ICP-MS and XPS analysis of the 1DBP cathodes based on the purified material (p-SWCNT) revealed a substantial decrease in iron metal contents to be approximately 1.2 wt% (compared to approximately 9.5 wt% in o-SWCNT), (Fig. S14a, Supplementary Information). Importantly, however, the complex purification process and series of metallic iron removal steps in the process caused a large loss in OER electrocatalytic performance in p-SWCNT (Fig. S13a, Supplementary Information).

Moreover, X-ray photoelectron spectroscopy analysis revealed that most residual iron metal

electrocatalysts were removed by the purification process (Fig. S14b, Supplementary Information, black curve), whereas absolutely pertained in o-SWCNT (Fig. S14b, Supplementary Information, red curve), which iron peaks evidently magnified in Fig. S14c (Fig. S14c, Supplementary Information). In addition, the residual iron metal electrocatalysts in both p-SWNT and o-SWNT were quantitatively measured by XPS measurement, which are 0.01 at% and 0.42 at%, respectively (Fig. S14d, Supplementary Information). This 1DBP cathodes presented were expected to exhibit unprecedented improvements in the electrochemical performance due to the structural/physicochemical uniqueness, which were difficult to realize with conventional HCF.

Furthermore, densely packed SWCNTs-reticulated distinctive structures allowed spacious active electrochemical reactive site surface area, which were directly related to electrocatalytic oxygen evolution/reduction reactions (OER/ORR), (Fig. 2c-d).⁵⁵⁻⁵⁶ Also, uniform SWCNT networks in 1DBP cathodes maximized the electronic conductivity, wherein evaluated to be 800 mS/cm of 1DBP cathodes compared to the 5 mS/cm of conventional HCF (Fig. 2e). In addition, the distinctive 1DBP cathodes' well-defined pathway immediately facilitated the electron/ion transport, which boosted electrochemical reaction kinetics of cells even at harsh operating conditions such as high charge/discharge current density. This unique nanomat 1DBP were employed as the bifunctional electrocatalyst embedded air-cathode for seawater batteries, and the electrochemical properties of the batteries were investigated by Galvanostatic charge-discharge experiment. Generally, the seawater batteries were assembled with different various air-electrodes, such as Pt/C, and Ir/C or carbon-based paper.

We compared the initial charge/discharge voltage profiles of the seawater batteries with different cathodes at a current density of 0.01 mA cm⁻² for 10 h at each step (Fig. 2f). The

battery containing the 1DBP cathodes exhibited significantly improved electrochemical performance compared that of the conventional HCF. The battery containing conventional HCF cathode without any electrocatalyst showed charge/discharge voltages of approximately 3.8 and 2.9 V, respectively, resulting in the substantial voltage gap (ΔV) between the charge/discharge voltage approximately 1.05 V. In contrast, the 1DBP cathode brought improved performance, lower charge/discharge voltages of approximately 3.5 and 2.9 V, respectively, following the significantly enhanced ΔV between the charge and discharge voltage approximately 0.6 V. These excellent bifunctional electrocatalytic performance improvements came from the electrocatalyst materials in cathode, o-SWCNT for ORR and residual iron metal oxide for OER, respectively. [57] The changes in the nominal charge/discharge voltage values and the voltage efficiency of the conventional HCF and 1DBP cells at each cycle are displayed in Figure 2g. The conventional HCF cell average charge/discharge voltages were about 3.79 and 2.92 V during 25 cycles, respectively, yielding a low voltage efficiency of approximately 76.9 %.

On the other hand, the 1DBP cathode cell exhibited enhanced average charge/discharge voltages were about 3.53 and 2.90 V for 25 cycles, respectively, resulting a high voltage efficiency of approximately 82.2 %. We attribute the outstanding performances dominantly to the superb electrocatalytic activity of the CNT and residual metallic iron.

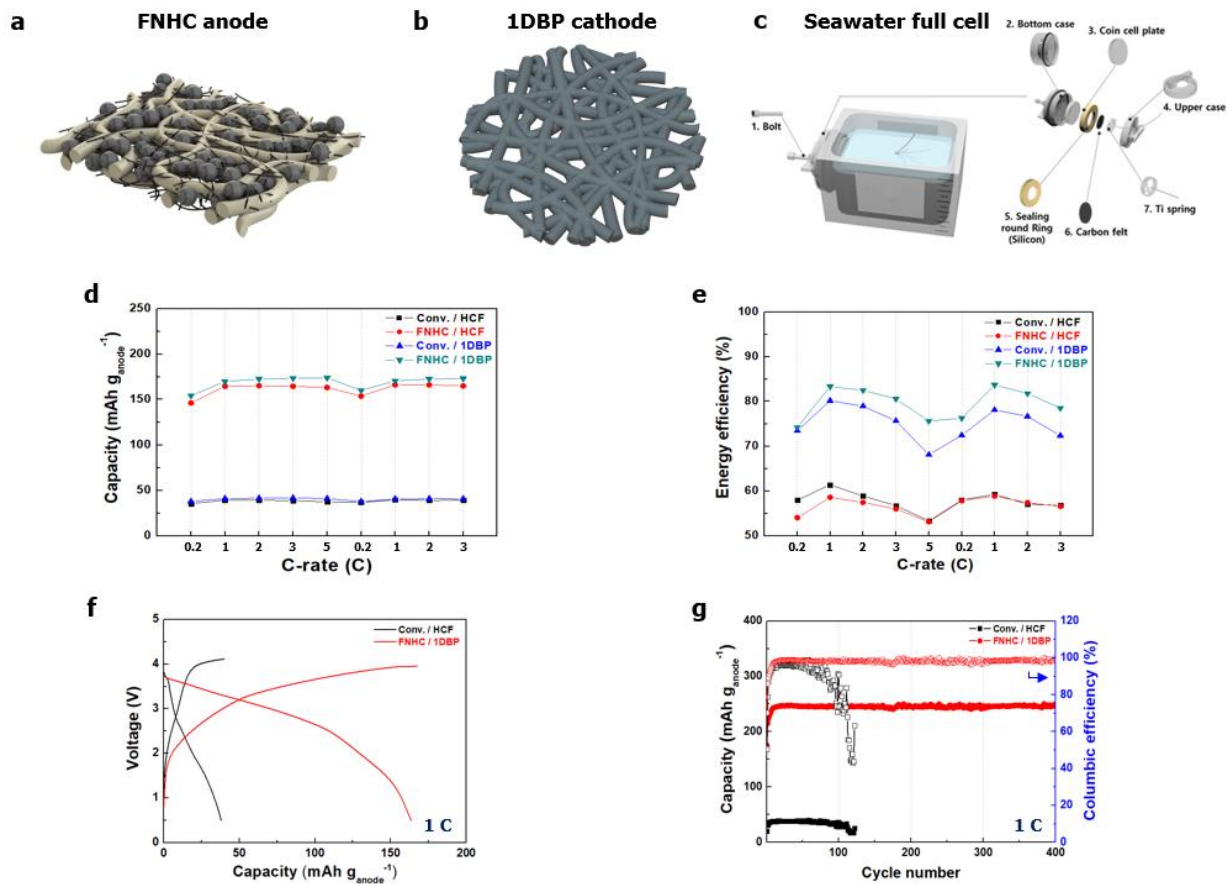


Fig. 3. Electrochemical performance of seawater full cells. (a) Schematic illustration of FNHC anode. (b) Schematic illustration of 1DBP cathode. (c) Schematic illustration of seawater full cell kit. (d) Discharge rate capability of seawater battery full cells with different cathode/anode combination at a charge/discharge current density was verified from 0.2 to 5.0 C, respectively. (e) Energy efficiency of seawater battery full cells during cycling. The charge/discharge current density was verified from 0.2 to 5.0 C, respectively. (f) Initial charge/discharge voltage profiles at charge/discharge current densities of 1.0 C/1.0 C of seawater full cells. (g) Cycling performance of seawater full cells at a charge/discharge current density of 1.0 C/1.0 C.

Electrochemical performance of FNHC/1DBP full cell

We fabricated a unique Na-metal-free seawater full cell containing FNHC anode and 1DBP cathode to ensure the safety, long-term cyclability, high energy and power densities (Fig. 3a-c). The electrochemical performance of a seawater battery was investigated using a kit-type full cell (1DBP cathode/NASICON/FNHC anode), (Fig. 3c).⁵⁷ In order to investigate each electrode's individual contribution in full cell system, we further scrutinized rate capability and energy efficiency of full cell. Figure 3d shows that the FNHC anode presented significantly higher discharge capacities than the conventional HC anodes over a wide range of charge/discharge current densities (from 0.2 to 5.0 C, respectively) in full cell. The well-designed 3D-bicontinuous electron/ion transport channels with elimination of the heavy metallic aluminum current collector conclusively contribute to this improvement in the discharge capacities and rate capability of the seawater full cell containing FNHC anodes.

Likewise, Figure 3e shows the contribution of 1DBP cathode to vastly higher energy efficiency than the conventional HCF cathodes over a wide range of charge/discharge current densities (from 0.2 to 5.0 C, respectively) in full cell. The vast electrochemically active surface area come from densely packed SWCNTs-reticulated distinctive structures and uniform SWCNT networks in 1DBP cathodes directly derives to this substantial energy efficiency advancement.

A distinctive achievement of the advanced hybrid electrode architecture application in seawater battery was the formidable capacity with highly enhanced energy efficiency, where the full cells were tested at a charge/discharge current density of 1.0 C/1.0 C (Fig. 3f). Figure 3f shows that the FNHC/1DBP cell presented substantially higher discharge capacities ($= 164 \text{ mAh g}_{\text{anode}}^{-1}$) than the control group Conv./HCF cell ($= 37 \text{ mAh g}_{\text{anode}}^{-1}$). In addition, the cycling

performance, where the seawater batteries were measured at a same charge/discharge current density of that (Fig. 3g). Figure 3g shows that the FNHC/1DBP full cell exhibited much higher discharge capacities and stable capacity retention during long-term cycling (99.99% after 400 cycles), whereas the control group Conv./HCF full cell suffered from a sharp capacity decay after only 100 cycles. These superior electrochemical performances (Energy density = 692 Wh kg⁻¹), (Power density = 3341 W kg⁻¹) of FNHC/1DBP seawater battery described above attributed to its exquisite advanced hybrid electrode architecture design.

DISCUSSION

In summary, we demonstrated advanced hybrid electrode architecture (FNHC anode/1DBP cathode) based on the 1D building block-interweaved hetero-nanomat frameworks seawater full cell battery system to overcome the limitation of ceramic separator. The advanced hybrid electrode architecture design is significantly facile and effective approach to enable high energy density and improve electrochemical kinetic. The FNHC anodes were fabricated via concurrent electrospinning and electrospinning, leading to the compact packing of HC powders in close contact with spatially interweaved polymeric nanofibers/CNT fibrous hetero-nanomat. As a result, 3D-bicontinuous ion/electron transport channels were uniformly developed inside the entire the electrodes. The highly reticulated CNT networks, contained in both structure of FNHC anodes and 1DBP cathodes, allowed for the elimination of metallic aluminum foil current collectors and providing well-interconnected electronic pathways within the electrodes. The FNHC/1DBP seawater battery full cell exhibited exceptional improvement (Energy density = 693 Wh kg⁻¹), (Power density = 3341 W kg⁻¹) in full cell performance and substantial

physicochemical mechanical property due to the durable polymeric framework, idiosyncratic chemical functionalities and distinctive structural merits of the hybrid hetero-nanomat framework electrodes, which were considerably difficult to achieve with conventional electrode technologies. We envisage that the advanced hetero-nanomat electrode architecture can be easily combined with a variety of electrode materials, eventually suggest to establishing new gateway to free platform for the development of advanced power sources in the incessant pursuit of high energy density.

MATERIALS AND METHODS

FNHC anode fabrication

The n-HC powders (average diameter = 10 μm) were dispersed in isopropyl alcohol (IPA) /deionized water (D.I. water) (=3/7 (w/w)) mixture solvent. The prepared dispersed solution containing hard-carbon nano-particles was mixed with SWCNTs wherein the ratio in composition of SWCNT/HC was 5/100 (w/w) and 0.4 wt% polyvinylpyrrolidone (PVP) was used as a dispersing agent for SWCNT.

Polyacrylonitrile (PAN) powders were dissolved in dimethyl formamide (DMF), wherein the concentration of PAN was 10 wt%. The hard-carbon/SWCNT mixture solution and the PAN solution were respectively projected to concurrent electrospaying/electrospinning through two different nozzles, thus producing n-HC particles embedded PAN/SWCNT FN electrodes sheet. After the PVP was removed by rinsing with D.I. water and followed ethanol, the nanomat electrode sheet was treated with calendaring process at room temperature and then thermally treated with 150 $^{\circ}\text{C}/2$ h and 120 $^{\circ}\text{C}/12$ h heating processes were followed for enhancing

chemical durability of PAN nanofibers and then.

1D bucky paper cathode fabrication

The SWCNTs and sodium dodecyl sulfate (SDS) was added as a dispersing agent (1 wt% in water as solvent). The SWCNTs suspension was poured into a filter paper located inside a Porcelain Buchner funnel and then subjected to vacuum infiltration, leading to the formation of 1DBP.

Electrochemical characterization for electrocatalysts

To study rotating ring disk electrode analysis, using concurrent by a potentiostat (Biologic, VMP3) with 1600 rpm controlled by a rotating disk electrode system (Biologic, RRDE-3A). A platinum wire and an (Hg/HgO vs. NHE is 0.140 V (NaOH, 1 M)) were used as the counter/reference electrodes, respectively. An aqueous solution of 0.1 M NaOH was used as the electrolyte. ORR curves were obtained on the disk electrode from a cathodic sweep from 0.1 V to -0.9 V (vs. Hg/HgO) at 10 mV s^{-1} after several cycles of CVs. Voltage of 0.4 V was applied to the ring electrode to estimate the amount of peroxide generated from the disk electrode. The anodic sweeps from 1.4 V to 1.8 V (vs. Hg/HgO) were presented as OER curves. The other conditions were the same as those applied for the ORR polarization curves. To demonstrate the stability of OER anodic and cathodic sweeps were repeated at 10 mV s^{-1} for 100 cycles.

Electrochemical characterization for conventional HC anode

Conventional hard-carbon (Conv.) anodes were prepared with hard-carbon (supplied from

Aekyung Petrochemical, Korea) as the active material, carbon black Super-P (TIMCAL) as the conductive additive, and polyvinylidene fluoride (PVdF, Alfa Aesar, USA) as the binder. Hard carbon, Super-P, and PVdF (80:10:10 in weight) slurries were prepared in N-Methyl-2-pyrrolidone (NMP), casted on aluminum foil, and dried at 80 °C under vacuum for 12 h. 1 M NaCF₃SO₃ in tetraethylene glycol dimethyl ether (TEGDME) was used as the electrolyte. Electrochemical performances of the hard carbon anodes were tested using 2032 coin cells, in which Na metal was used as the counter electrode and reference electrode, and recorded by an automatic galvanostatic charge-discharge unit, PNE battery cycler (PNE Solution), in the voltage range of 0.00-2.00 V (vs. Na/Na⁺) at 25 °C. During the initial two cycles in all tests, charge/discharge were performed at 0.1C (25 mA g⁻¹) for the stabilization process. The rate capability was evaluated at charging/discharging current densities of 0.2C (50 mA g⁻¹), 1C (250 mA g⁻¹), 2C (500 mA g⁻¹), 3C (750 mA g⁻¹), 5C (1250 mA g⁻¹) for each of five cycles. The cyclabilities were evaluated at 2 types of charging/discharging current densities of 0.2C and 3C. The capacities were calculated based on the total weight of anode including conductive additive, binder, and current collector. Also, the specific capacities were calculated based on the mass of the HC.

Electrochemical characterization for cathode

Heated carbon felt (HCF)⁵⁸ and 1D building block bucky paper (1DBP) were used as the cathode for evaluating the seawater cathode half-cell, respectively. Natural seawater was obtained from Ilsan beach, Ulsan, Republic of Korea (35°29'49.2"N 129°25'51.6"E).⁵⁹ Seawater coin cells, seawater cell testers, and Na-ion conducting solid electrolytes (Na₃Zr₂Si₂PO₁₂, NASICON) were supplied from 4 TO ONE Energy Co., Ltd, Korea. In the seawater half-cells, the Na metal was applied as the anode and the 1 M NaCF₃SO₃ in TEGDME

was used as the anolyte. The cells were prepared in a glove box with less than 0.1 ppm of both oxygen and moisture. Seawater cathode half cells were tested at a current density of 0.02 mA cm⁻² for 10 hours in each charging/discharging steps. All electrochemical tests were carried out on the same cycler, WBCS3000 battery cycler (WonATech. Co., Korea).

Electrochemical characterization for seawater full cell

The electrochemical performance tests of the seawater full-cells were compared by combination of anodes (Conv. and FNHC) and cathodes (HCF and 1DBP), respectively. All electrochemical tests were carried out on the same cycler, WBCS3000 battery cycler (WonATech. Co., Korea). During the initial two cycles in all tests, they were charged at a current density of 0.1C (25 mA g⁻¹) and a capacity cut-off (250 mAh g⁻¹), followed by discharging down to 0.50 V for the stabilization process. The cyclabilities were evaluated by charging at a current density of 1C (250 mA g⁻¹) and a capacity cut-off (250 mAh g⁻¹), followed by discharging down to 0.50 V. And, the rate capabilities of the seawater full-cells were examined by charging and discharging at the same current densities of 0.2C, 1C, 2C, 3C, and 5C for each of five cycles. As in the Na-ion half-cell case, the capacities were calculated based on the total mass of anode.

SUPPLEMENTARY INFORMATIONS

Fig. S1. Morphology of (a) bare hard carbon and (b) nano hard carbon particles. (c) XRD patterns of hard carbons.

Fig. S2. Composition ratio analysis of FNHC anode. (a) XPS atomic weight integral of FNHC anode. (b) Polymer etching test of FNHC anode.

Fig. S3. Morphology of (a) Conv. HC anode. (b) FNHC anode.

Fig. S4. N₂ adsorption-desorption isotherm of anodes.

Fig. S5. Electrolyte wettability of anodes.

Fig. S6. Areal mass of anodes.

Fig. S7. (a) Digital camera images of anode suspension along SWCNTs contents. (b) Apparent viscosity of anode suspension along SWCNTs contents. (c) Electrical conductivity of anode suspension along SWCNTs contents. (d) Electrical conductivity of anodes.

Fig. S8. Electrochemical performance of anode half-cell. (a) rate capability of anodes (= capacity per active material mass (mAh g_{HC}⁻¹). (b) High current density (3.0 C) cyclability of anodes (= capacity per active material mass (mAh g_{HC}⁻¹). (c) (0.2 C) Cyclability of anodes (= capacity per active material mass (mAh g_{HC}⁻¹). (d) (0.2 C) Cyclability of anodes (= capacity per anode mass (mAh g_{anode}⁻¹).

Fig. S9. N₂ adsorption-desorption isotherm of cathodes.

Fig. S10. Morphology of conventional HCF.

Fig. S11. Confocal-Raman of SWCNTs.

Fig. S12. TGA profiles of SWCNTs

Fig. S13. RRDE OER profiles of cathodes.

Fig. S14. (a) ICPMS of SWCNTs. (b) XPS full spectra of SWCNTs. (c) XPS Fe 2p spectra of SWCNTs. (d) XPS atomic weight integral of SWCNTs.

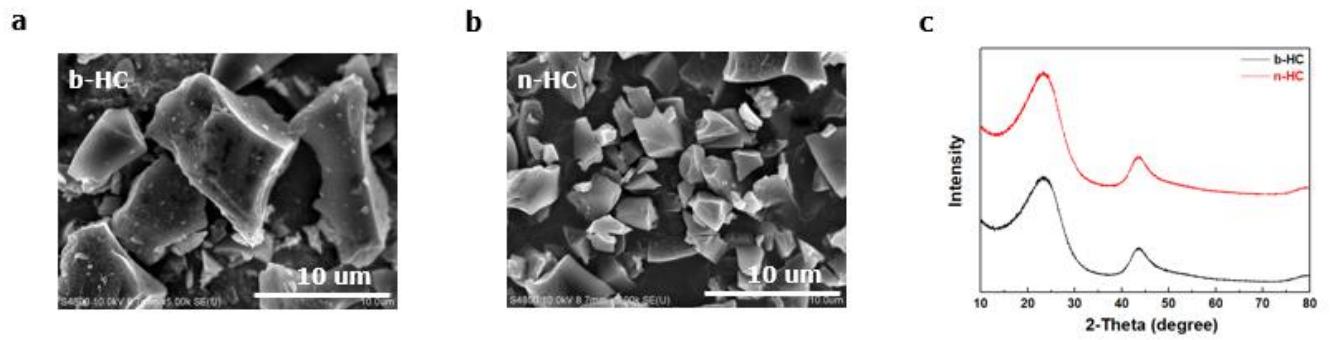


Fig. S1. Morphology of (a) bare hard carbon and (b) nano hard carbon particles. (c) XRD patterns of hard carbons.

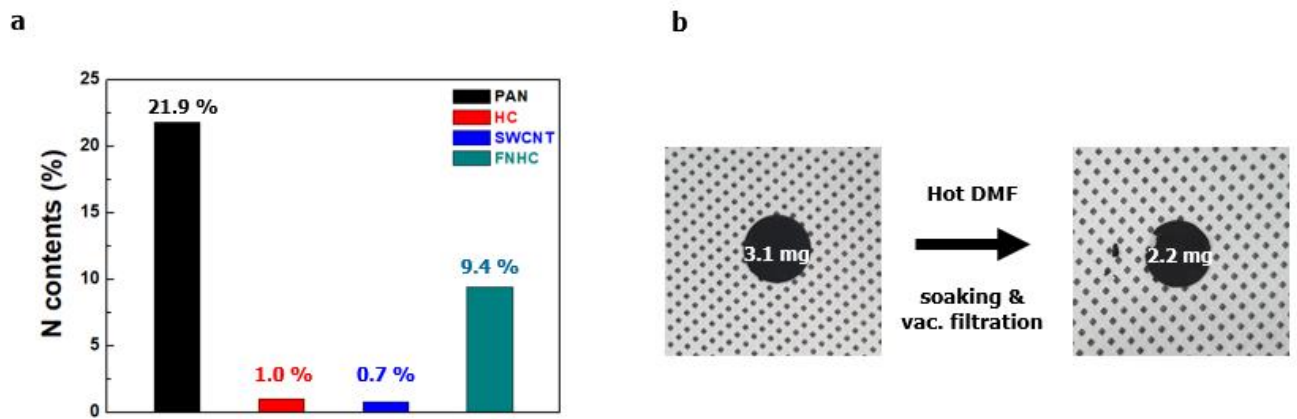


Fig. S2. Composition ratio analysis of FNHC anode. (a) XPS atomic weight integral of FNHC anode. (b) Polymer etching test of FNHC anode.

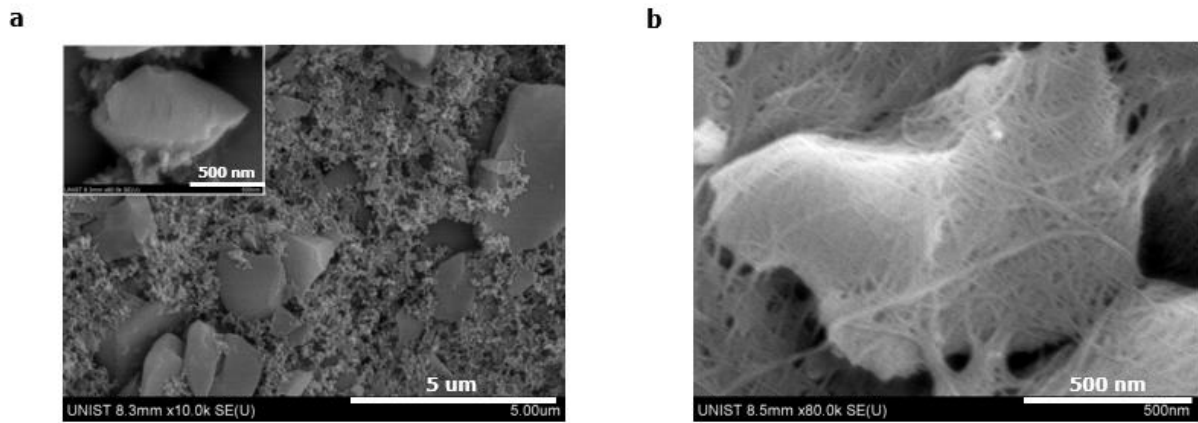


Fig. S3. Morphology of (a) Conv. HC anode. (b) FNHC anode.

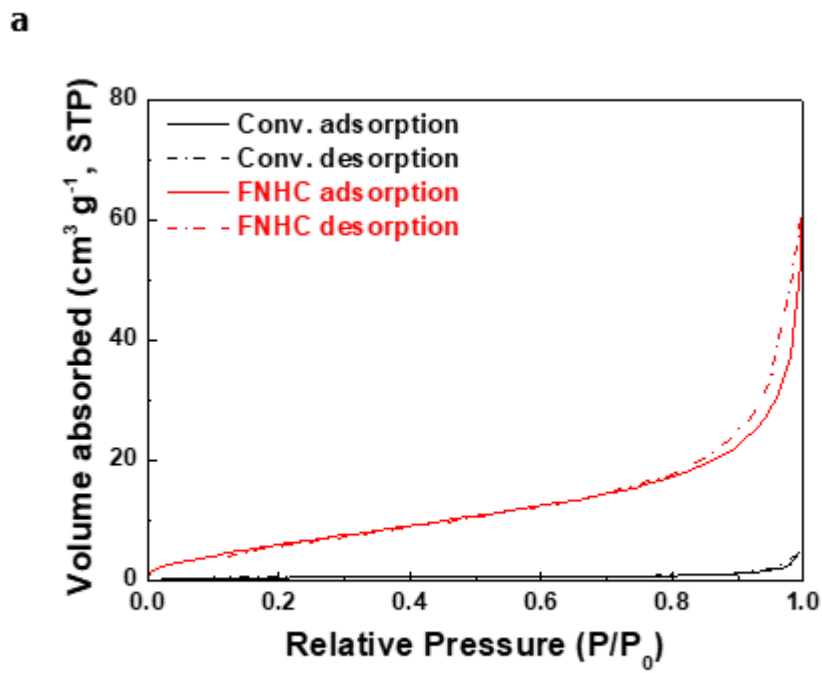


Fig. S4. N₂ adsorption-desorption isotherm of anodes.

a

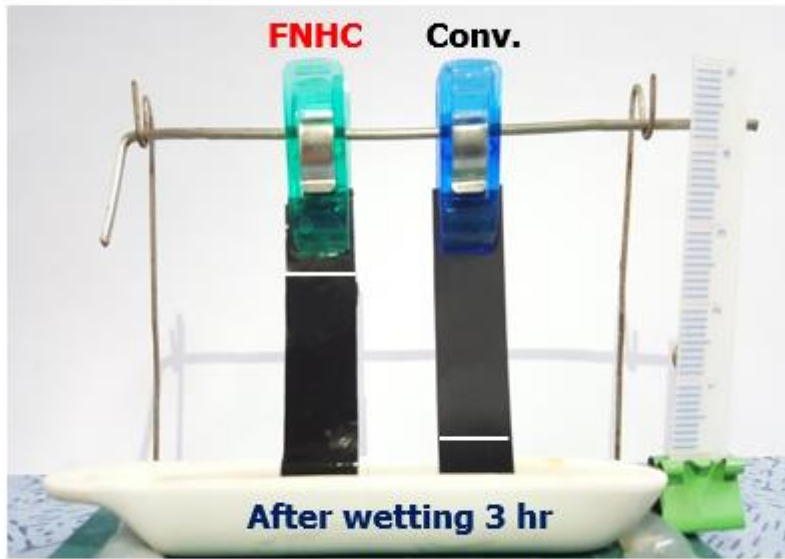


Fig. S5. Electrolyte wettability of anodes.

a

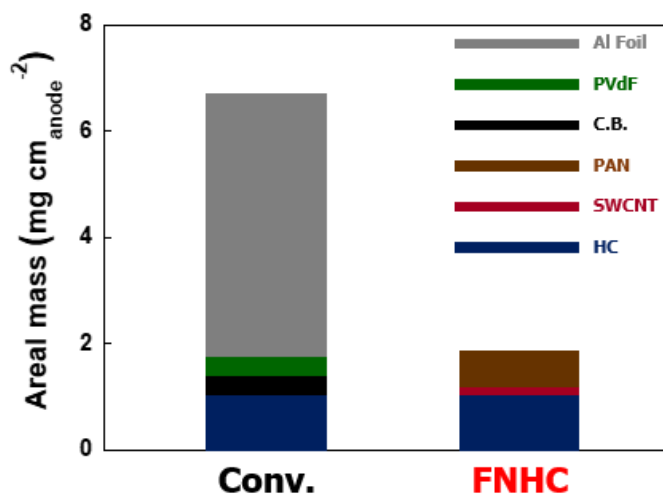


Fig. S6. Areal mass of anodes.

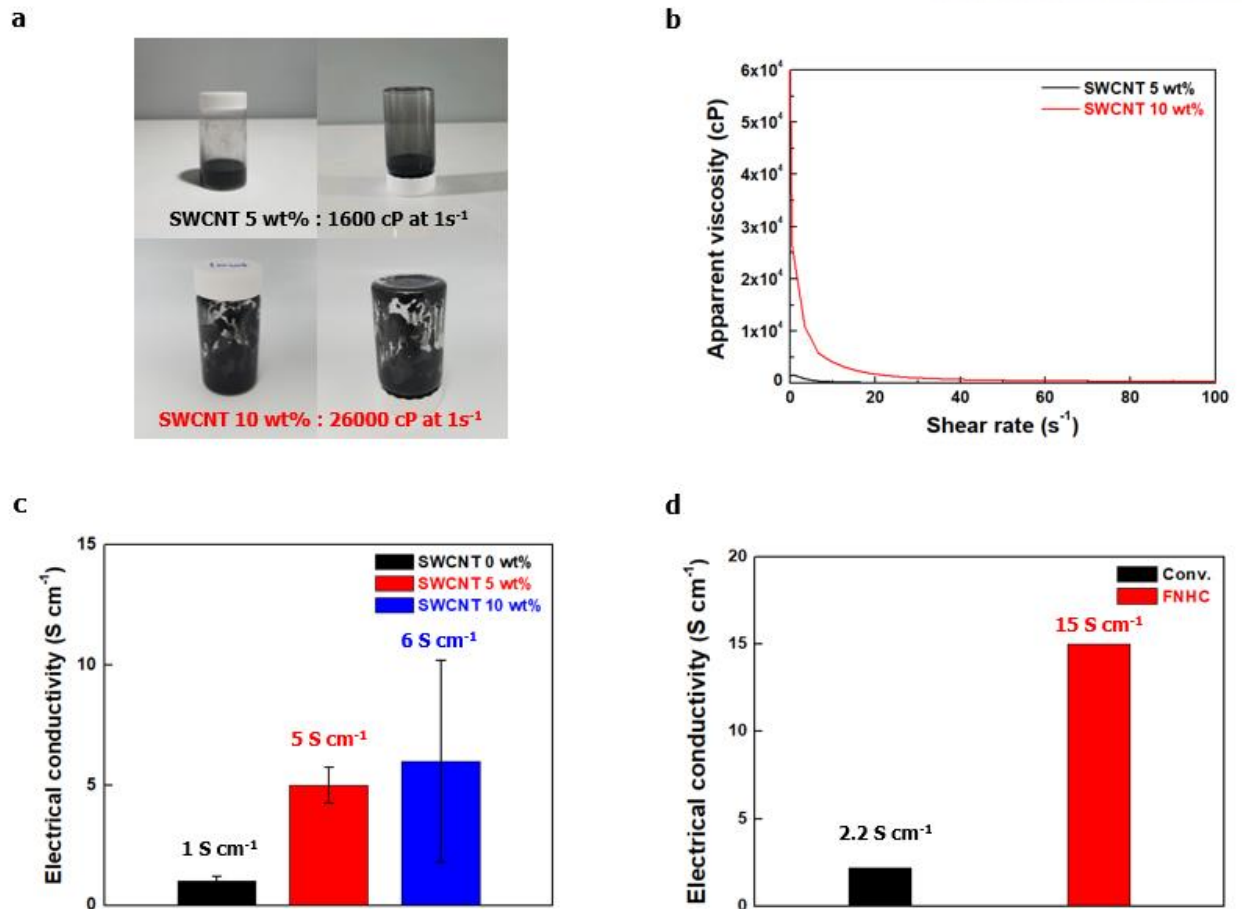


Fig. S7. (a) Digital camera images of anode suspension along SWCNTs contents. **(b)** Apparent viscosity of anode suspension along SWCNTs contents. **(c)** Electrical conductivity of anode suspension along SWCNTs contents. **(d)** Electrical conductivity of anodes.

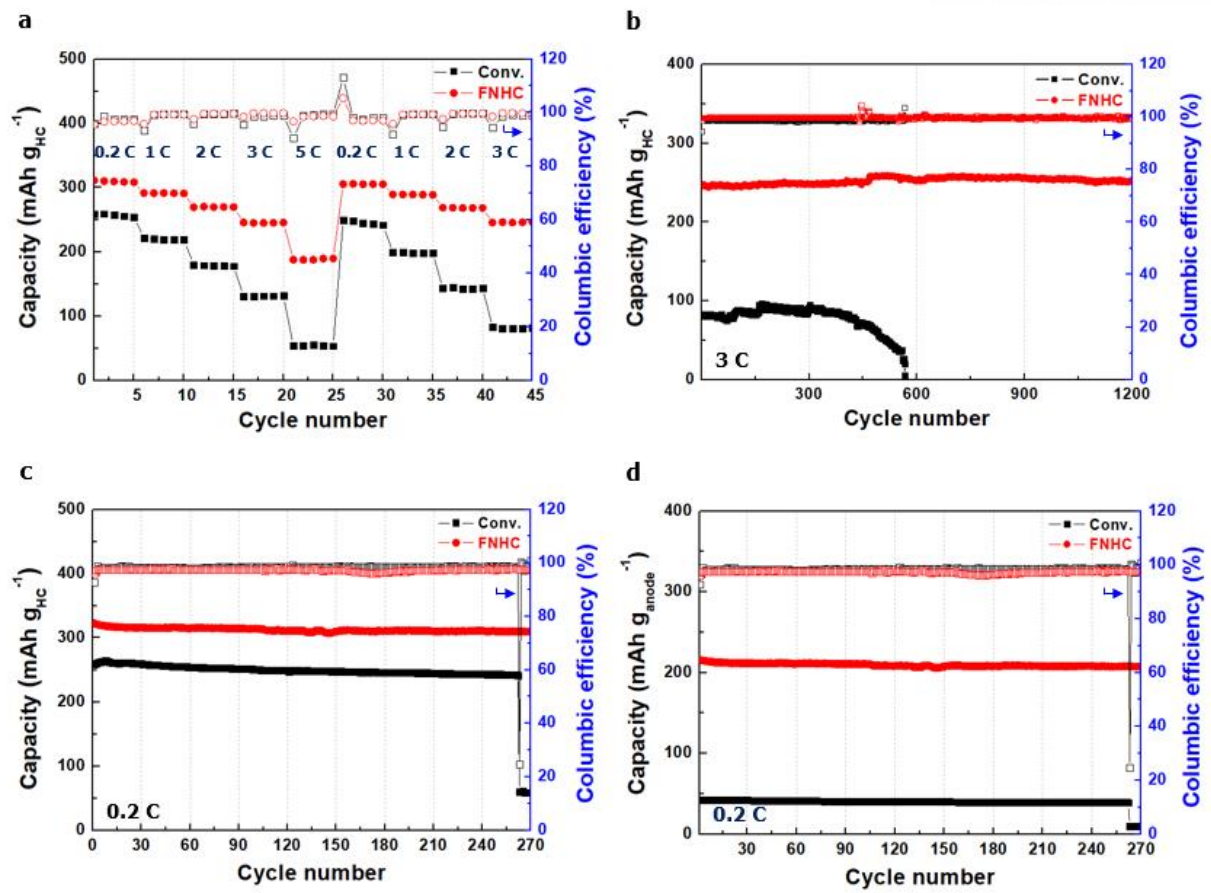


Fig. S8. Electrochemical performance of anode half-cell. **(a)** rate capability of anodes (= capacity per active material mass (mAh g_{HC}⁻¹). **(b)** High current density (3.0 C) cyclability of anodes (= capacity per active material mass (mAh g_{HC}⁻¹). **(c)** (0.2 C) Cyclability of anodes (= capacity per active material mass (mAh g_{HC}⁻¹). **(d)** (0.2 C) Cyclability of anodes (= capacity per anode mass (mAh g_{anode}⁻¹).

a

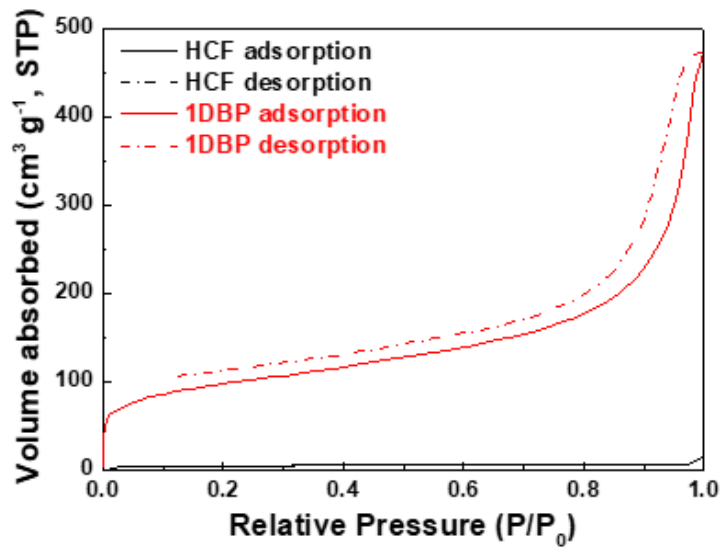


Fig. S9. N₂ adsorption-desorption isotherm of cathodes.

a

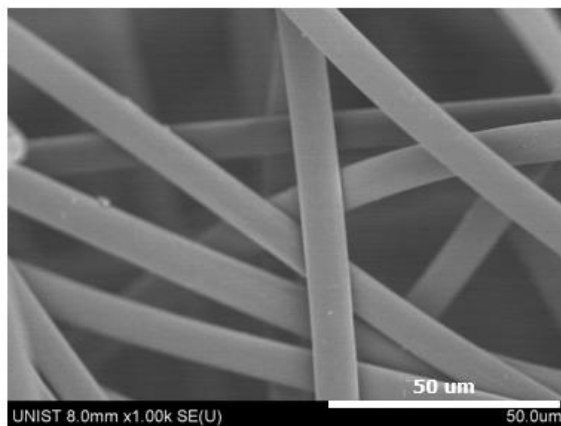


Fig. S10. Morphology of conventional HCF.

a

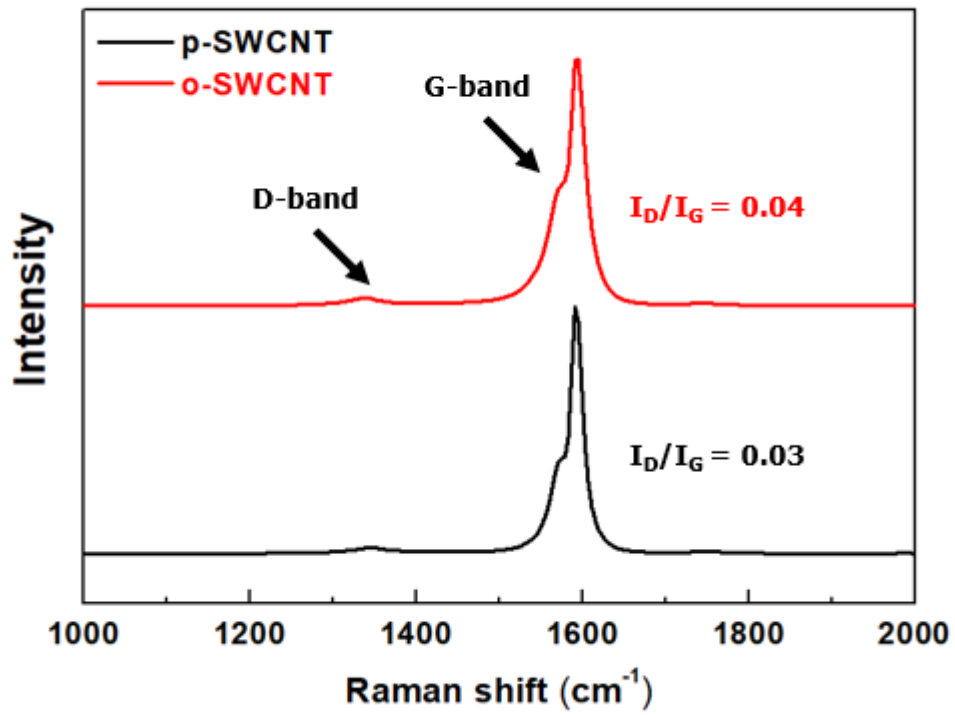


Fig. S11. Confocal-Raman of SWCNTs.

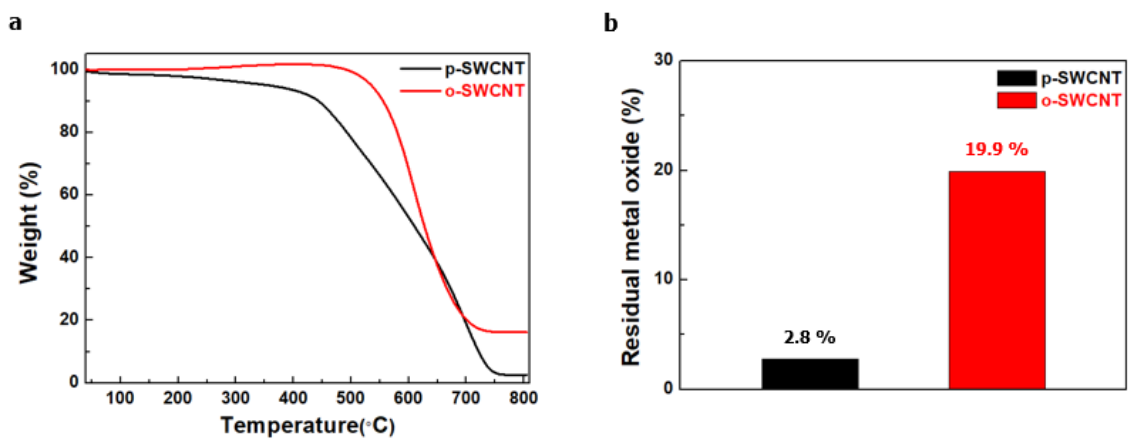


Fig. S12. TGA profiles of SWCNTs.

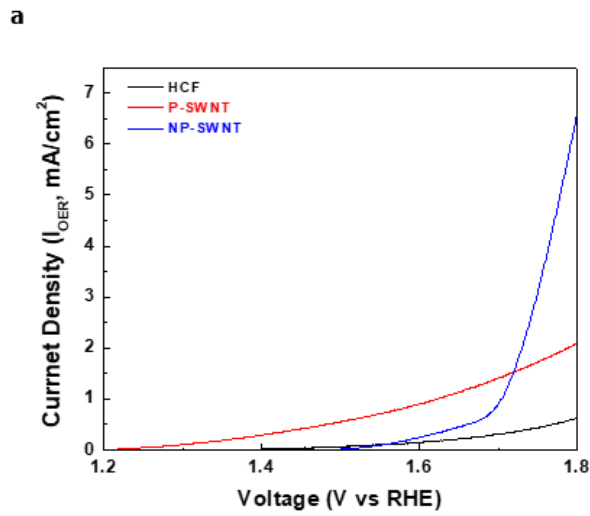


Fig. S13. (a) RRDE OER current profiles of cathodes.

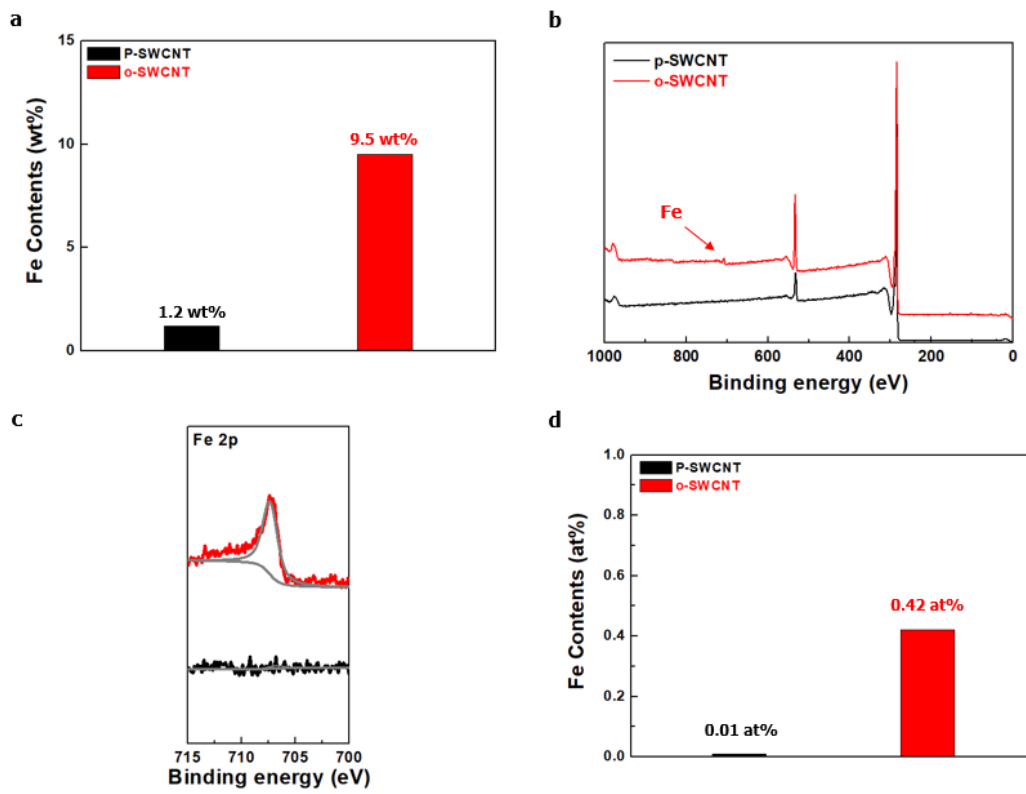


Fig. S14. (a) ICPMS of SWCNTs. (b) XPS full spectra of SWCNTs. (c) XPS Fe 2p spectra of SWCNTs. (d) XPS atomic weight integral of SWCNTs.

REFERENCES AND NOTES

- Dunn, B.; Kamath, H.; Tarascon, J. M., Electrical energy storage for the grid: a battery of choices. *Science* **2011**, *334* (6058), 928-35.
- Liu, C.; Li, F.; Ma, L. P.; Cheng, H. M., Advanced materials for energy storage. *Adv. Mater.* **2010**, *22* (8), E28-62.
- Tarascon, J. M.; Armand, M., Issues and challenges facing rechargeable lithium batteries. *Nature* **2001**, *414* (6861), 359-67.
- Cheng, F.; Liang, J.; Tao, Z.; Chen, J., Functional materials for rechargeable batteries. *Adv. Mater.* **2011**, *23* (15), 1695-715.
- Palomares, V.; Serras, P.; Villaluenga, I.; Hueso, K. B.; Carretero-González, J.; Rojo, T., Na-ion batteries, recent advances and present challenges to become low cost energy storage systems. *Energy & Environmental Science* **2012**, *5* (3), 5884.
- Yoo, H. D.; Shterenberg, I.; Gofer, Y.; Gershinshy, G.; Pour, N.; Aurbach, D., Mg rechargeable batteries: an on-going challenge. *Energy & Environmental Science* **2013**, *6* (8), 2265.
- Peng, Z.; Freunberger, S. A.; Chen, Y.; Bruce, P. G., A reversible and higher-rate Li-O₂ battery. *Science* **2012**, *337* (6094), 563-6.
- Truong, T. T.; Qin, Y.; Ren, Y.; Chen, Z.; Chan, M. K.; Greeley, J. P.; Amine, K.; Sun, Y., Single-crystal silicon membranes with high lithium conductivity and application in lithium-air batteries. *Adv. Mater.* **2011**, *23* (42), 4947-52.
- Hartmann, P.; Bender, C. L.; Vracar, M.; Durr, A. K.; Garsuch, A.; Janek, J.; Adelhelm, P., A rechargeable room-temperature sodium superoxide (NaO₂) battery. *Nat Mater* **2013**, *12* (3), 228-32.
- He, H.; Niu, W.; Asl, N. M.; Salim, J.; Chen, R.; Kim, Y., Effects of aqueous electrolytes on the voltage behaviors of rechargeable Li-air batteries. *Electrochim. Acta* **2012**, *67*, 87-94.
- Kundu, D.; Talaie, E.; Duffort, V.; Nazar, L. F., The emerging chemistry of sodium ion batteries for electrochemical energy storage. *Angew. Chem. Int. Ed. Engl.* **2015**, *54* (11), 3431-48.
- Clément, R. J.; Bruce, P. G.; Grey, C. P., Review—Manganese-Based P2-Type Transition Metal Oxides as Sodium-Ion Battery Cathode Materials. *J. Electrochem. Soc.* **2015**, *162* (14), A2589-A2604.
- Slater, M. D.; Kim, D.; Lee, E.; Johnson, C. S., Sodium-Ion Batteries. *Adv. Funct. Mater.* **2013**, *23* (8), 947-958.
- Han, M. H.; Gonzalo, E.; Singh, G.; Rojo, T., A comprehensive review of sodium layered oxides: powerful cathodes for Na-ion batteries. *Energy & Environmental Science* **2015**, *8* (1), 81-102.
- Ponrouch, A.; Marchante, E.; Courty, M.; Tarascon, J.-M.; Palacín, M. R., In search of an optimized electrolyte for Na-ion batteries. *Energy & Environmental Science* **2012**, *5* (9), 8572.
- Kim, J.-K.; Mueller, F.; Kim, H.; Bresser, D.; Park, J.-S.; Lim, D.-H.; Kim, G.-T.; Passerini, S.; Kim, Y., Rechargeable-hybrid-seawater fuel cell. *NPG Asia Materials* **2014**, *6* (11), e144.
- Santhanagopalan, D.; Qian, D.; McGilvray, T.; Wang, Z.; Wang, F.; Camino, F.; Graetz, J.; Dudney, N.; Meng, Y. S., Interface Limited Lithium Transport in Solid-State Batteries. *J*

- Phys Chem Lett* **2014**, 5 (2), 298-303.
18. Kim, J.-K.; Lim, Y. J.; Kim, H.; Cho, G.-B.; Kim, Y., A hybrid solid electrolyte for flexible solid-state sodium batteries. *Energy & Environmental Science* **2015**, 8 (12), 3589-3596.
 19. Inaguma, Y.; Liqan, C.; Itoh, M.; Nakamura, T.; Uchida, T.; Ikuta, H.; Wakihara, M., High ionic conductivity in lithium lanthanum titanate. *Solid State Commun.* **1993**, 86 (10), 689-693.
 20. Wang, Y.-J.; Pan, Y.; Kim, D., Conductivity studies on ceramic Li_{1.3}Al_{0.3}Ti_{1.7}(PO₄)₃-filled PEO-based solid composite polymer electrolytes. *J. Power Sources* **2006**, 159 (1), 690-701.
 21. Kobayashi, Y., All-solid-state lithium secondary battery with ceramic/polymer composite electrolyte. *Solid State Ionics* **2002**, 152-153, 137-142.
 22. Nairn, K.; Forsyth, M.; Every, H.; Greville, M.; MacFarlane, D. R., Polymer-ceramic ion-conducting composites. *Solid State Ionics* **1996**, 86-88, 589-593.
 23. Inda, Y.; Katoh, T.; Baba, M., Development of all-solid lithium-ion battery using Li-ion conducting glass-ceramics. *J. Power Sources* **2007**, 174 (2), 741-744.
 24. Zheng, H.; Li, J.; Song, X.; Liu, G.; Battaglia, V. S., A comprehensive understanding of electrode thickness effects on the electrochemical performances of Li-ion battery cathodes. *Electrochim. Acta* **2012**, 71, 258-265.
 25. Ha, D. H.; Islam, M. A.; Robinson, R. D., Binder-free and carbon-free nanoparticle batteries: a method for nanoparticle electrodes without polymeric binders or carbon black. *Nano Lett.* **2012**, 12 (10), 5122-30.
 26. Wang, K.; Luo, S.; Wu, Y.; He, X.; Zhao, F.; Wang, J.; Jiang, K.; Fan, S., Super-Aligned Carbon Nanotube Films as Current Collectors for Lightweight and Flexible Lithium Ion Batteries. *Adv. Funct. Mater.* **2013**, 23 (7), 846-853.
 27. Chao, D.; Xia, X.; Liu, J.; Fan, Z.; Ng, C. F.; Lin, J.; Zhang, H.; Shen, Z. X.; Fan, H. J., A V₂O₅/conductive-polymer core/shell nanobelt array on three-dimensional graphite foam: a high-rate, ultrastable, and freestanding cathode for lithium-ion batteries. *Adv. Mater.* **2014**, 26 (33), 5794-800.
 28. Fang, X.; Ge, M.; Rong, J.; Zhou, C., Free-standing LiNi_{0.5}Mn_{1.5}O₄/carbon nanofiber network film as lightweight and high-power cathode for lithium ion batteries. *ACS Nano* **2014**, 8 (5), 4876-82.
 29. Chen, Z.; To, J. W. F.; Wang, C.; Lu, Z.; Liu, N.; Chortos, A.; Pan, L.; Wei, F.; Cui, Y.; Bao, Z., A Three-Dimensionally Interconnected Carbon Nanotube-Conducting Polymer Hydrogel Network for High-Performance Flexible Battery Electrodes. *Advanced Energy Materials* **2014**, 4 (12), 1400207.
 30. Chen, Z.; Yuan, Y.; Zhou, H.; Wang, X.; Gan, Z.; Wang, F.; Lu, Y., 3D nanocomposite architectures from carbon-nanotube-threaded nanocrystals for high-performance electrochemical energy storage. *Adv. Mater.* **2014**, 26 (2), 339-45.
 31. Kim, J.-M.; Park, C.-H.; Wu, Q.; Lee, S.-Y., 1D Building Blocks-Intermingled Heteronanomats as a Platform Architecture For High-Performance Ultrahigh-Capacity Lithium-Ion Battery Cathodes. *Advanced Energy Materials* **2016**, 6 (2), 1501594.
 32. Kim, J.-M.; Kim, J. A.; Kim, S.-H.; Uhm, I. S.; Kang, S. J.; Kim, G.; Lee, S.-Y.; Yeon, S.-H.; Lee, S.-Y., All-Nanomat Lithium-Ion Batteries: A New Cell Architecture Platform for Ultrahigh Energy Density and Mechanical Flexibility. *Advanced Energy Materials* **2017**, 7 (22), 1701099.
 33. Jabbour, L.; Destro, M.; Gerbaldi, C.; Chaussy, D.; Penazzi, N.; Beneventi, D., Aqueous processing of cellulose based paper-anodes for flexible Li-ion batteries. *J. Mater. Chem.*

- 2012, 22 (7), 3227.
34. Leijonmarck, S.; Cornell, A.; Lindbergh, G.; Wågberg, L., Single-paper flexible Li-ion battery cells through a paper-making process based on nano-fibrillated cellulose. *Journal of Materials Chemistry A* **2013**, 1 (15), 4671.
 35. Lin, D.; Lu, Z.; Hsu, P.-C.; Lee, H. R.; Liu, N.; Zhao, J.; Wang, H.; Liu, C.; Cui, Y., A high tap density secondary silicon particle anode fabricated by scalable mechanical pressing for lithium-ion batteries. *Energy & Environmental Science* **2015**, 8 (8), 2371-2376.
 36. Hasan, T.; Scardaci, V.; Tan, P.; Rozhin, A. G.; Milne, W. I.; Ferrari, A. C., Stabilization and “Debundling” of Single-Wall Carbon Nanotube Dispersions in N-Methyl-2-pyrrolidone (NMP) by Polyvinylpyrrolidone (PVP). *The Journal of Physical Chemistry C* **2007**, 111 (34), 12594-12602.
 37. Gupta, A. K.; Singhal, R. P.; Agarwal, V. K., Effect of heat treatment on dielectric relaxation of polyacrylonitrile: Reversible thermally induced structural change. *J. Appl. Polym. Sci.* **1981**, 26 (11), 3599-3608.
 38. Gupta, A. K.; Maiti, A. K., Effect of heat treatment on the structure and mechanical properties of polyacrylonitrile fibers. *J. Appl. Polym. Sci.* **1982**, 27 (7), 2409-2416.
 39. Cho, S.-J.; Choi, K.-H.; Yoo, J.-T.; Kim, J.-H.; Lee, Y.-H.; Chun, S.-J.; Park, S.-B.; Choi, D.-H.; Wu, Q.; Lee, S.-Y.; Lee, S.-Y., Hetero-Nanonet Rechargeable Paper Batteries: Toward Ultrahigh Energy Density and Origami Foldability. *Adv. Funct. Mater.* **2015**, 25 (38), 6029-6040.
 40. Choi, K. H.; Cho, S. J.; Chun, S. J.; Yoo, J. T.; Lee, C. K.; Kim, W.; Wu, Q.; Park, S. B.; Choi, D. H.; Lee, S. Y.; Lee, S. Y., Heterolayered, one-dimensional nanobuilding block mat batteries. *Nano Lett.* **2014**, 14 (10), 5677-86.
 41. Wei, T.-S.; Fan, F. Y.; Helal, A.; Smith, K. C.; McKinley, G. H.; Chiang, Y.-M.; Lewis, J. A., Biphasic Electrode Suspensions for Li-Ion Semi-solid Flow Cells with High Energy Density, Fast Charge Transport, and Low-Dissipation Flow. *Advanced Energy Materials* **2015**, 5 (15), 1500535.
 42. Islam, M. F.; Rojas, E.; Bergey, D. M.; Johnson, A. T.; Yodh, A. G., High Weight Fraction Surfactant Solubilization of Single-Wall Carbon Nanotubes in Water. *Nano Lett.* **2003**, 3 (2), 269-273.
 43. Luo, S.; Wang, K.; Wang, J.; Jiang, K.; Li, Q.; Fan, S., Binder-free LiCoO₂/carbon nanotube cathodes for high-performance lithium ion batteries. *Adv. Mater.* **2012**, 24 (17), 2294-8.
 44. Zhang, H.-X.; Feng, C.; Zhai, Y.-C.; Jiang, K.-L.; Li, Q.-Q.; Fan, S.-S., Cross-Stacked Carbon Nanotube Sheets Uniformly Loaded with SnO₂ Nanoparticles: A Novel Binder-Free and High-Capacity Anode Material for Lithium-Ion Batteries. *Adv. Mater.* **2009**, 21 (22), 2299-2304.
 45. Gui, Z.; Zhu, H.; Gillette, E.; Han, X.; Rubloff, G. W.; Hu, L.; Lee, S. B., Natural cellulose fiber as substrate for supercapacitor. *ACS Nano* **2013**, 7 (7), 6037-46.
 46. Hu, L.; Wu, H.; La Mantia, F.; Yang, Y.; Cui, Y., Thin, flexible secondary Li-ion paper batteries. *ACS Nano* **2010**, 4 (10), 5843-8.
 47. Kim, J.-H.; Kim, J.-H.; Choi, E.-S.; Yu, H. K.; Kim, J. H.; Wu, Q.; Chun, S.-J.; Lee, S.-Y.; Lee, S.-Y., Colloidal silica nanoparticle-assisted structural control of cellulose nanofiber paper separators for lithium-ion batteries. *J. Power Sources* **2013**, 242, 533-540.
 48. Arora, P.; Zhang, Z., Battery Separators. *Chem. Rev.* **2004**, 104 (10), 4419-4462.
 49. Kim, H.; Lim, H. D.; Kim, S. W.; Hong, J.; Seo, D. H.; Kim, D. C.; Jeon, S.; Park, S.; Kang, K., Scalable functionalized graphene nano-platelets as tunable cathodes for high-

- performance lithium rechargeable batteries. *Sci Rep* **2013**, *3*, 1506.
50. Lim, H. D.; Song, H.; Kim, J.; Gwon, H.; Bae, Y.; Park, K. Y.; Hong, J.; Kim, H.; Kim, T.; Kim, Y. H.; Lepro, X.; Ovalle-Robles, R.; Baughman, R. H.; Kang, K., Superior rechargeability and efficiency of lithium-oxygen batteries: hierarchical air electrode architecture combined with a soluble catalyst. *Angew. Chem. Int. Ed. Engl.* **2014**, *53* (15), 3926-31.
 51. Li, Y.; Zhou, W.; Wang, H.; Xie, L.; Liang, Y.; Wei, F.; Idrobo, J. C.; Pennycook, S. J.; Dai, H., An oxygen reduction electrocatalyst based on carbon nanotube-graphene complexes. *Nat Nanotechnol* **2012**, *7* (6), 394-400.
 52. Narlikar, A. V.; Fu, Y. Y.; Collins, P. G., DEFECTS AND DISORDER IN CARBON NANOTUBES **2017**, *1*.
 53. Yoo, J.; Ju, Y.-W.; Jang, Y.-R.; Gwon, O.; Park, S.; Kim, J.-M.; Lee, C. K.; Lee, S.-Y.; Yeon, S.-H.; Kim, G.; Lee, S.-Y., One-pot surface engineering of battery electrode materials with metallic SWCNT-enriched, ivy-like conductive nanonets. *Journal of Materials Chemistry A* **2017**, *5* (24), 12103-12112.
 54. Lehman, J. H.; Terrones, M.; Mansfield, E.; Hurst, K. E.; Meunier, V., Evaluating the characteristics of multiwall carbon nanotubes. *Carbon* **2011**, *49* (8), 2581-2602.
 55. Senthilkumar, S. T.; Park, S. O.; Kim, J.; Hwang, S. M.; Kwak, S. K.; Kim, Y., Seawater battery performance enhancement enabled by a defect/edge-rich, oxygen self-doped porous carbon electrocatalyst. *Journal of Materials Chemistry A* **2017**, *5* (27), 14174-14181.
 56. Gwon, O.; Kim, C.; Kwon, O.; Jeong, H. Y.; Park, H.-K.; Shin, J.; Ju, Y.-W.; Kim, G., An Efficient Oxygen Evolution Catalyst for Hybrid Lithium Air Batteries: Almond Stick Type Composite of Perovskite and Cobalt Oxide. *J. Electrochem. Soc.* **2016**, *163* (9), A1893-A1897.
 57. Abirami, M.; Hwang, S. M.; Yang, J.; Senthilkumar, S. T.; Kim, J.; Go, W. S.; Senthilkumar, B.; Song, H. K.; Kim, Y., A Metal-Organic Framework Derived Porous Cobalt Manganese Oxide Bifunctional Electrocatalyst for Hybrid Na-Air/Seawater Batteries. *ACS Appl Mater Interfaces* **2016**, *8* (48), 32778-32787.
 58. Han, J.; Hwang, S. M.; Go, W.; Senthilkumar, S. T.; Jeon, D.; Kim, Y., Development of coin-type cell and engineering of its compartments for rechargeable seawater batteries. *J. Power Sources* **2018**, *374*, 24-30.
 59. Hwang, S. M.; Kim, J.; Kim, Y.; Kim, Y., Na-ion storage performance of amorphous Sb₂S₃nanoparticles: anode for Na-ion batteries and seawater flow batteries. *J. Mater. Chem. A* **2016**, *4* (46), 17946-17951.